



Accessibility and strength of H-acceptor hydroxyls of ordered mesoporous silicas probed by pyridine donor

Mayara R. Alves¹ · Mateus F. Paiva¹ · Pablo T. A. Campos¹ · Elon F. de Freitas¹ · Maria Clara H. Clemente¹ · Gesley Alex V. Martins¹ · Alceu T. Silveira Jr.² · Luis C. Cides da Silva³ · Marcia C. A. Fantini³ · Sílvia C. L. Dias¹ · José A. Dias¹

Accepted: 7 October 2020 / Published online: 13 October 2020
© Springer Science+Business Media, LLC, part of Springer Nature 2020

Abstract

Ordered mesoporous silica (OMS) is an important and useful material for a variety of applications, including catalysis, adsorption, sensing and controlled drug delivery. The surface chemistry and the silanol groups on OMS pores are key properties for the potential modification and application of this material. This research aimed to synthesize (using standard protocols) and differentiate the accessibility and strength of the H-acceptor Si–OH from FDU-12, SBA-16, MCM-41 and SBA-15 by pyridine (Py) donor, where the first two have cubic pore structures and the last two have hexagonal pore structures. Donor–acceptor properties were assessed by calculation of the surface Si–OH densities by thermogravimetry (TG), H₂O-TPD/MS, and ²⁹Si MAS and CP/MAS NMR. The nature of the Si–OH groups on these materials was determined to be hydrogen-bonding sites using FT-IR spectroscopy of Py adsorption. The reactivity of these silanol groups was probed by Py-TG and slurry microcalorimetry of Py adsorption in cyclohexane. Differences in accessibility and reactivity were discussed considering the total potential sites on the surface (n_{OH}) versus the actual sites that can react with the Py molecule (n_{Py}). By using microcalorimetry, it was possible to quantitatively distinguish the strength of the sites: The acidity order was approximately the same as the relative amount of silanol groups (Si–OH) and Py on the surface of the OMS materials (α_{Py}): FDU-12 > MCM-41 \geq SBA-16 > SBA-15.

Keywords Ordered mesoporous silica (OMS) · Microcalorimetry of pyridine adsorption · Water-TPD/MS · Thermogravimetry · Accessibility to Si–OH · Strength of silanol groups

1 Introduction

A breakthrough was achieved in the 1990s with the syntheses of nanostructured materials with large mesopores (2 nm < diameter < 50 nm), which are known as ordered mesoporous silica (OMS) and named the M41S family: MCM-41, MCM-48 and MCM-50 [1, 2]. This discovery revealed a variety of possible applications in catalysis, adsorption, sensing, and controlled drug transportation, among others, which immediately triggered many research

groups to study these new mesoporous materials. The number of published synthetic processes was so large that it was mandatory to certify reliable and reproducible methods to obtain these new OMS materials [3–5] and benefit nonexperts in this field. The expected applications of these materials rely primarily on the properties of the siloxane and the variety and distribution of silanol groups on the OMS surface. This is expected to affect the development of different modifications, such as the introduction of a metal (e.g., Al, Ni, V) to enhance the acidity in different reactions in which pure OMS is inactive [6–10].

Another important application involves modification of the OMS adsorption capacity. The expected loading efficiency will depend on the size of the adsorbate, as well as the pore size of the OMS adsorbent [11]. Applications involving enzyme adsorption are reported to be strongly affected by the electrostatic interactions between the enzyme and OMS, with a crucial dependence on the isoelectric point of the enzyme

Electronic supplementary material The online version of this article (<https://doi.org/10.1007/s10934-020-00994-x>) contains supplementary material, which is available to authorized users.

✉ José A. Dias
jdias@unb.br; josediasunb@gmail.com
<http://www.labcat.unb.br>

Extended author information available on the last page of the article

[12]. The electrostatic forces on the OMS surface rest on the combination of their siloxane and silanol groups. Thus, quantitative information on the location and strength of the silanol groups on OMS is very significant for adsorption studies [11, 12]. Additionally, many OMS structures have been studied in recent years for their potential as drug transportation and delivery systems, which rely on the adsorption capacity of these materials. Thus, many revisions and papers have been published confirming these correlations [12–18].

Although considerable progress has been made in the synthesis and characterization of these porous materials, much less emphasis has been placed on the accessibility and mainly silanol acceptor capacity of mesoporous silica. The literature has many data on MCM-41 and SBA-15 accessibility, for example [19, 20], but little or no data are available for others (e.g., FDU-12 and SBA-16). The accessibility and donor–acceptor capacity of such OMS silanols are key properties for their modifications and further applications. Several techniques, such as Fourier transform infrared (FT-IR) spectroscopy, temperature-programmed desorption (TPD), solid-state nuclear magnetic resonance (MAS NMR), and calorimetric-adsorption (Cal-Ad) method by means of probe molecules (e.g., NH_3 , Py, CO), have been used to reveal the acidity properties of different materials [21–23]. These properties are accessibility, nature, strength, quantity, and distribution of active sites, which in most cases are measured as a function of the donor–acceptor interaction [22]. Because the donor–acceptor strength of surface groups may change substantially with structure and morphology, there is always a demand for knowledge about those parameters [10, 14].

Thus, the aim of this research was to synthesize using standard protocols of the literature and investigate the H-acceptor capacity of four OMS types (FDU-12, SBA-16, MCM-41 and SBA-15) by means of a donor molecule. These four OMSs were chosen to analyze the influence of the pore structure properties (cubic and hexagonal structures and specific surface areas) on acidity. This characterization involved the investigation of structural and acidity properties, which were studied by FT-IR, small-angle X-ray scattering (SAXS), ^{29}Si MAS and CP/MAS NMR spectroscopy, low-temperature adsorption/desorption of N_2 (-196°C), thermogravimetry (TG), TPD of water or pyridine followed by continuous mass spectrometry (TPD/MS), and microcalorimetry in liquid-phase pyridine adsorption. The accessibility and reactivity are discussed.

2 Experimental

2.1 Syntheses of ordered mesoporous silicas

Syntheses of all the OMS materials (FDU-12, SBA-16, MCM-41 and SBA-15) followed standard procedures from

the literature with a few modifications [5, 22, 24–27]. All reagents were analytical grade and used without any further purification and included aqueous ammonia (NH_4OH , 28–30%, Vetec), hydrochloric acid (HCl , 37%, Vetec), tetraethylorthosilicate (TEOS, 98%, Sigma–Aldrich), cetyltrimethylammonium chloride (CTAC, Sigma–Aldrich), 1,3,5-trimethylbenzene (TMB, Aldrich), Pluronic P123 (Aldrich), Pluronic 127 (Aldrich), anhydrous pyridine (99.8%, Aldrich), KCl (99.9%, Vetec), deionized water (Merck Millipore, Milli-Q, model direct 8), and N_2 or synthetic air ($\text{O}_2 + \text{N}_2$, with $20 \pm 0.5\%$ O_2), where both special gases 5.0 were obtained from White Martins/Praxair Inc. The detailed procedures are described in the Electronic Supplementary Material.

2.2 Structural characterization of OMS

The OMS materials were structurally characterized by FT-IR, SAXS, TEM, ^{29}Si MAS and CP/MAS NMR spectroscopy, and adsorption and desorption of N_2 gas at low temperature (-196°C) for textural analysis. A detailed description of these characterizations is provided in the Electronic Supplementary Material.

2.3 Measurements of accessibility and donor–acceptor properties

The OMS materials were studied using the following techniques: desorption of water or pyridine by thermogravimetry (TG), temperature programmed desorption of water or pyridine followed by mass spectrometry (TPD/MS), and microcalorimetry in liquid-phase with pyridine adsorption.

The H_2O -TPD and Py-TPD experiments were performed on a TA Instruments thermal analyzer (model SDT 2960) using Pt crucibles and the following program under N_2 flow (110 mL min^{-1}): heating ramp at $10^\circ\text{C min}^{-1}$ up to 100°C , isothermal treatment at 100°C for 30 min, and heating ramp at $10^\circ\text{C min}^{-1}$ from 100 up to 950°C . Pyridine was preadsorbed onto the OMS materials according to the procedure described in the Electronic Supplementary Material. Once the samples with adsorbed pyridine were prepared, they were stored in a glove bag with N_2 and analyzed immediately by TG/DTG. The number of OH groups (n_{OH}) was quantitatively calculated in the samples, without pyridine, by water desorption, according to the calculations described in the literature [28, 29]. The number of pyridine molecules bonded to the silanol groups (n_{Py}) was quantitatively determined by analysis of the mass loss of the materials before and after pyridine adsorption, taking into consideration the hydration of each sample. The method developed in our laboratory [30] is detailed in the Supplementary Material.

The H_2O -TPD/MS and Py-TPD/MS experiments were performed by means of a temperature-programmed

desorption reactor coupled with a mass spectrometer (TPD/MS). The reaction system obtained from Altamira Instruments (AMI-90R) has and consisted of a TCD detector coupled to a Dycor Ametek mass spectrometer (range 0–100 m/e) with continuous and simultaneous detection in up to eight channels. The OMS material (100 mg) was placed in a "U"-shaped quartz reactor tube that was inserted into the furnace of the equipment. The TPD experiment was performed using the following program: (i) the OMS was dried at 100 °C (25 to 100 °C, heating ramp of 10 °C min⁻¹) for a total of 60 min under N₂ flow at 20 cm³ min⁻¹; (ii) a heating ramp of 10 °C min⁻¹ was applied under N₂ flow of 10 cm³ min⁻¹ up to 950 °C. The reaction products were monitored via their respective mass fragments (m/e): 18 and 17 (base peak and additional peak of water); 79, 78, 52 and 51 (base peak and additional peaks of pyridine; according to NIST Webbook [31]). In all cases, the peak at m/e = 28 (N₂) was used as a reference for the background.

Liquid-phase microcalorimetry of pyridine in cyclohexane slurries was used to measure the evolved heat and to calculate the enthalpies of OMS (FDU-12, SBA-16, MCM-41, and SBA-15). All prepared OMS materials were activated at 200 °C for 4 h before the experiments. A diluted pyridine solution (0.100 mol L⁻¹) in cyclohexane was added by titration to the solid slurry in anhydrous cyclohexane using a calibrated gas-tight syringe (Hamilton, 5 mL), and the heat evolved was determined in an isoperibol calorimeter (model ISC 4300, Calorimetry Sciences Corporation). The thermal bath of the calorimeter was regulated at 28.0000 °C before starting the experiment. Samples (0.5 g) of OMS were weighed and transferred to an isothermal calorimetric cell, followed by the addition of 25 mL of anhydrous cyclohexane. These operations were carried out in a dry nitrogen glove box. The pyridine solution was added incrementally (e.g., 0.05 mL per injection) to the slurry at intervals of 4 min, which was sufficient to the system equilibrate. The heat of diluted pyridine added to cyclohexane was measured separately and considered negligible for the heating system. The equivalent energy of the system was measured by a calibration curve before and after each titration.

3 Results and discussion

3.1 Basic structural and textural characterizations of OMS

The successful syntheses of OMS materials could be proven by different standard methods that are used in the literature, such as FT-IR, SAXS, textural analysis by N₂ adsorption, TEM, and ²⁹Si MAS and CP/MAS NMR. A detailed description and discussion of these characterization techniques is provided in the Supplementary Material. However, SAXS

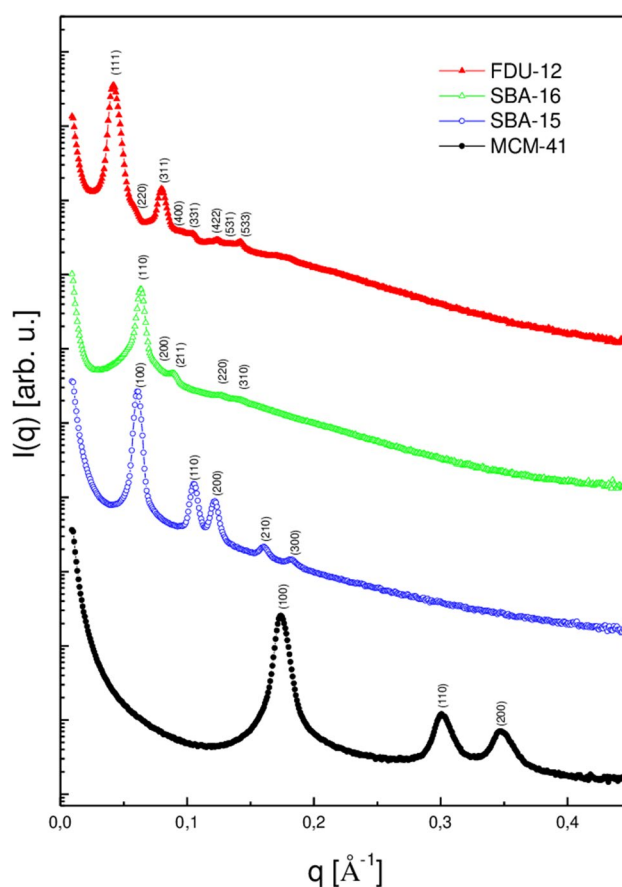


Fig. 1 SAXS patterns of the OMS materials FDU-12, SBA-16, SBA-15, and MCM-41, with displaced intensities on a logarithmic scale

is presented with more detailed explanation to demonstrate the correct synthetic procedure and a brief description of the other results is also included for the sake of clarity.

The FT-IR spectra of calcined OMS materials showed the characteristic absorptions of the silica framework vibrations (Fig. S1), in agreement with the literature [8, 22, 28]. The bands at approximately 1640 cm⁻¹ and 3450 cm⁻¹ were attributed to the presence of adsorbed water molecules on the silanol surface. Generally, these bands are not specific to different silicas and are independent of their structure.

The SAXS patterns of the mesoporous silicas are shown in Fig. 1. All samples display typical diffraction peaks, confirming the ordered structural arrangement of pores. The SAXS diffraction pattern of the FDU-12 sample exhibits eight characteristic peaks that can be attributed to the indexed reflections (111), (220), (311), (400), (331), (442), (531) and (533) of a cubic structure with *Fm3m* symmetry, indicating successful synthesis [25]. In the curve for MCM-41, three peaks, corresponding to the indexed reflections (100), (110) and (200), are observed. The (100) plane shows high intensity, and its position was observed to shift to lower 2θ after the removal of the

template and subsequent condensation of silanol groups [5, 22]. The last two reflections confirm that the synthesized material was composed of a highly ordered bidimensional hexagonal arrangement of pores in space group $P6mm$. Regarding the SBA-15 material, five Bragg reflections were observed, indexed as the (100), (110), (200), (210) and (300) diffraction facets. The occurrence of these reflections corresponds to the mesoporous silica whose diffraction signals are attributed to the periodic arrangement of the parallel channels, suggesting the formation of a mesostructured solid with bidimensional hexagonal $P6mm$ symmetry [26]. The structure of SBA-16 is characterized by a three-dimensional network of cage-like pores arranged in a cubic structure with body-centered symmetry connected through small mesopores. The results of the SAXS analysis indicate that the obtained SBA-16 had well-resolved diffraction patterns, suggesting an ordered mesostructure representative of the cubic space group Imm [26, 27, 32], where the (110), (211), (220) and (310) reflections are present. The unit cell parameters (a_0), which are the distances between the centers of two adjacent pores, are correlated with the values of q (100) and d (100) that were calculated according to the literature [33].

The textural properties of the OMS materials were examined by low-temperature nitrogen sorption isotherms and pore size distribution (Fig. S2-A and B) using the Brunauer–Emmett–Teller (BET), t-plot, and NLDFT (non-local density functional theory) models.

All isotherms were predominately type IV(a), consistent with mesoporous materials with different hysteresis behaviors, but a contribution of microporosity (type I) is also evident, with a high N_2 adsorption at low relative pressures ($p/p^0 < 0.1$). In the region of relative pressure values $0.2 < p/p^0 < 0.95$, adsorption of the second and third layers of N_2 occurred, which was accompanied by the characteristic capillary condensation in the mesopores at $p/p^0 \approx 0.65$, 0.42, and 0.43 for SBA-15, FDU-12 and SBA-16, respectively. For MCM-41, the important adsorption at low p/p^0 is considered mainly due to monolayer coverage of the pore walls [1]. These observations agree with IUPAC classification [34].

About hysteresis behaviors, practically no hysteresis was observed for MCM-41, because of small width pores (~ 4 nm), which is typical of materials with ordered uniform pores [1, 2, 34]. In the case of SBA-15 with hexagonal pore structure, the isotherms present a similar profile, but now it shows hysteresis type H1 loop, which is associated with porous materials composed of ordered uniform pores, but larger than those of MCM-41. SBA-15 showed type H1 loop characteristic of narrow range of mesopores. FDU-12 and SBA-16 samples exhibit type H2(a). This type of hysteresis is associated with different mechanisms of condensation and evaporation in pores with a narrow neck and broad body (cage-like pores, pore entrances narrower than cages). All

those behaviors are compatible with standard samples in the literature [5].

The main properties of the investigated samples are summarized in Table 1. The total pore volume (V_{tot}) for isotherms of type IV(a) can be obtained at a relative pressure close to unity (e.g., $p/p^0 = 0.98$) by assuming the pores filled with nitrogen in the liquid state (i.e., application of Gurvich rule). The pore volume calculated by NLDFT ($V_{p(DFT)}$) is fair close to V_{tot} confirming that the model employed is well fitted. In addition, it can be observed that the calculated microporous area has contributed to the total area of OMS materials, as well as the volume of micropores in V_{tot} . Thus, an overview of the contribution of the micropore parameters clearly shows a significant role in the distribution of silanols on the accessible surface. It is known that micropores originate high silanol group concentration (hydroxyl nests), which may be accessible by different probe molecules [35].

Transmission electron microscopy (TEM) is an essential technique for investigating the structures of materials. It can produce images that are the projections of three-dimensional structure and contain crystallographic information. Fig. S3 shows the images of the synthesized OMS materials (i.e., FDU-12, SBA-16, MCM-41 and SBA-15). TEM images show the mesoporous structures, in addition to fringes that are a consequence of different interactions between the electron beam and the ordered pores, which can be hexagonal, square, etc. generating the image pattern with high or low absorption. The detailed analysis of the images confirmed the proper syntheses of hexagonal pores in MCM-41 and

Table 1 Unit cell parameters obtained by SAXS and textural properties from N_2 adsorption/desorption isotherms at -196 °C

OMS/parameter	FDU-12	SBA-16	MCM-41	SBA-15
a_0 (nm) ^a	25.9 ± 2.7	14.01 ± 0.02	4.18 ± 0.01	11.92 ± 0.07
S_{BET} (m ² /g) ^b	672	705	1109	684
S_{Mic} (m ² /g) ^c	184	300	205	187
S_{Mes} (m ² /g) ^d	488	405	904	497
V_{tot} (cm ³ /g) ^e	0.56	0.48	0.85	1.05
$V_{p(DFT)}$ (cm ³ /g) ^f	0.52	0.40	0.83	0.92
V_{Mic} (cm ³ /g) ^g	0.22	0.13	0.19	0.09
V_{Mes} (cm ³ /g) ^h	0.34	0.35	0.66	0.96

^aCalculated according to the literature [33]

^bSpecific surface area obtained by the BET method in the p/p^0 range of 0.02 to 0.2. The standard error (2σ) was ± 10 m²/g

^cMicroporous surface area obtained by the t-plot method

^dMesoporous surface area was obtained by the $S_{BET} - S_{Mic}$

^eTotal pore volume calculated by the amount of gas adsorbed at $p/p^0 = 0.98$

^fPore volume calculated by NLDFT Model

^gMicropore volume calculated by t-plot

^hMesopore volume calculated by $V_{tot} - V_{Mic}$

SBA-15 and the cubic space group of FDU-12 and SBA-16, according to the literature [5, 24].

Solid-state ^{29}Si NMR is an important tool for silicon chemical environment determination in different silicates [5, 36], confirming the species formation designated Q^4 [$\text{Si}(\text{OSi})_4$], Q^3 [$\text{Si}(\text{OSi})_3(\text{OH})$], and Q^2 [$\text{Si}(\text{OSi})_2(\text{OH})_2$]. Fig. S4 shows the ^{29}Si MAS NMR spectra of calcined FDU-12, SBA-16, MCM-41, and SBA-15, as well as the respective deconvolutions, providing more specific information regarding species Q^4 , Q^3 and Q^2 [32, 33, 36, 37]. The relative intensities attributed to the different Q^n groups are presented in Table 2. Among the studied OMS materials, FDU-12 showed the highest concentration of Q^3 and Q^2 species or SiOH groups, whereas SBA-15 presented the lowest SiOH concentration. The lower amount of Q^3 and Q^2 species in the mesoporous silicas may indicate a lower number and accessibility of these OH groups. The correlation of these parameters to the strength and accessibility of Si–OH groups will be further discussed. In addition, ^{29}Si CP/MAS NMR spectra of OMS materials (Fig. S5) were obtained and confirmed the presence of Q^2 and Q^3 silicon sites [38].

3.2 Acidity of synthesized OMS materials

3.2.1 Accessibility of sites by temperature programmed water desorption

First, it is important to understand and demonstrate the accessibility of the acid sites of a molecular sieve. Once an OMS material is prepared, calcined, and exposed to a certain atmosphere (humidity, for instance), the silicon chemical environment will be created. Thermal and/or vacuum treatments will change the amount and distribution of surface silanol and siloxane groups on silica-based materials [39–41]. In this sense, the use of H_2O -TPD/MS is very advantageous because the water signal ($m/e = 18$) can be monitored by mass spectrometry. The pattern of H_2O -TPD/MS of the molecular sieves is shown in Fig. 2. All OMS materials showed the same general behavior: (i) the first signal (between 110 and 300 °C) is associated with desorption

of surface water from the Si–OH of the most condensed structure (i.e., bridge silanols); (ii) the second signal is associated with the dehydroxylation between the remaining silanol groups, mainly the isolated silanols, generating siloxanes and water ($\text{Si–OH}\cdots\text{OH–Si} \rightarrow \text{Si–O–Si} + \text{H}_2\text{O}$) [19, 42]. It should be noted that the OMS materials were pretreated at 100 °C under dry N_2 for 2 h before these measurements.

The presence of different Si–OH groups on the surface of silica and OMS materials has been extensively studied in the literature by FT-IR, mainly DRIFTS. We observed (Fig S6) two main bands in the range of $3767\text{--}3700\text{ cm}^{-1}$ related to O–H vibrations from isolated Si–OH groups and a broader band at 3600 cm^{-1} assigned to surface silanol groups with hydrogen bonds (bridge silanols) [43–45]. The positions of these bands may shift slightly depending on the nature of the silica material and demonstrate the presence of different silanol groups on it.

The nature of Si–OH groups was also probed by a combination of ^{29}Si and ^1H - ^{29}Si CP/MAS NMR experiments for each OMS. It has been shown by ^1H - ^{29}Si CP/MAS NMR that geminal and free Si–OH groups can be promptly discriminated (Q^2 and Q^3 environments) and are not affected by the presence of water molecules for quantification purposes [46, 47]. The Si–OH groups are more influenced by the surfactant used, which forms a hydration layer on the interface surfactant-silica wall [48]. The results of fitting the experimental spectra clearly showed that two of the three chemical environments of the OMS are related to silicon nuclei that are coupled to nearby protons. The areas under the deconvoluted signals are directly proportional to the species of the respective structural units of the sample, which allowed calculation of the relative proportion of silicon

Table 2 ^{29}Si MAS NMR relative magnitudes of Q^n environments obtained by deconvolution using the composite Gaussian–Lorentzian function (Origin v 8.0)

OMS	Q^4	Q^3	Q^2	SiOH (%) ^a	CD ^b
FDU-12	77	22	1	24	0.77
SBA-16	81	17	2	21	0.81
MCM-41	80	18	2	22	0.80
SBA-15	85	11	4	19	0.85

^aRelative amount of silanol groups (mol\% Si) = $[(2\text{Q}^2 + \text{Q}^3)/(\text{Q}^2 + \text{Q}^3 + \text{Q}^4)] \times 100$

^bCondensation degree (CD) = $\text{Q}^4/(\text{Q}^2 + \text{Q}^3 + \text{Q}^4)$ [35]

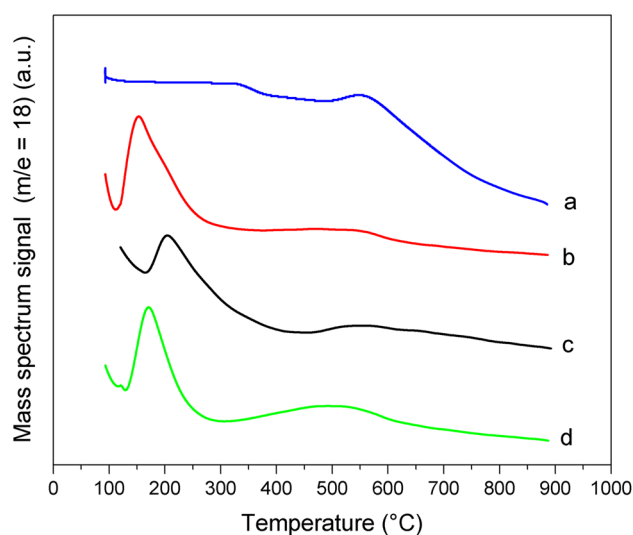


Fig. 2 H_2O -TPD/MS curves for the OMS: (a) SBA-15; (b) FDU-12; (c) MCM-41, (d) SBA-16

environments (Table 2) and the molar percentage of silanol groups [32, 33, 36, 37]. For all studied OMS materials under our experimental protocol synthesis and calcination conditions, the integrated relative intensities of the signals indicated that most of the silicon atoms belong to Q^4 substructures ($>77\%$), whereas Q^2 environments had the lowest concentration ($<4\%$). Among the studied OMS, FDU-12 showed the highest concentration of Q^3 and Q^2 species and SiOH groups (24%) and consequently the lowest condensation degree (0.77), whereas SBA-15 presented the lowest SiOH concentration (19%) and the highest condensation degree (0.85). It is important to keep in mind that the relative amount of the respective environments of Si–OH is an indication of distribution and not of the relative strength.

A quantitative measurement of the total Si–OH groups on the OMS was performed by the thermogravimetric method, which has been largely conducted in the literature [29, 48, 49]. Thus, using the proposed equations [29] and based on the Zhuravlev model, the total number of OH groups was determined (Table 3). As observed in Fig. 2, according to the H_2O -TPD/MS experiments performed on these OMSs, only water was released from the heating treatment.

The n_{OH} value represents the maximum number of sites that each OMS can provide and be accessed by a suitable probe molecule to directly react with. A suitable probe has an appropriate size and conditions of adsorption. The n_{OH} is an important parameter that may drive the design of any modified OMS material. It can be noted that the obtained data in Table 3 are close to some other values calculated under approximately the same conditions of preparation and calcination (e.g., 3.6 and 3.5 mmol g^{-1} for MCM-41 and SBA-15, respectively, but a larger difference were found for SBA-16, 8.3 mmol g^{-1}) [28, 35]. It should also be noted that the n_{OH} data for FDU-12 were not found in the literature. Nonetheless, these data should be carefully considered because there are a variety of silanol density data in the literature, mainly due to different experimental methods of preparation, calcination, calculation and the chosen stage boundary point, discussed by Zhuravlev [39], which have been pointed out in the literature [28, 35, 50]. If one looks at literature, no systematic procedure can be found for OMS

materials to calculate silanol densities. The accessibility for Py probe (columns 4 and 5) will be discussed in the next section.

3.2.2 Accessibility of sites by pyridine and acid strength

First, the nature of the silanol interaction with pyridine was examined by two methods: (i) FT-IR of adsorbed pyridine and (ii) gas-phase dehydration of ethanol. The FT-IR spectra (Fig. 3) of FDU-12, SBA-16, MCM-41 and SBA-15 clearly showed that the sites present on these OMSs formed practically only hydrogen bonds with pyridine; i.e., they function much more as H-acceptors than H-donors through py interaction. The main absorption bands are located at 1489 and 1447 cm^{-1} . The absence of a clear band at approximately 1540 cm^{-1} confirms that no Brønsted sites (proton donor) are present on these samples. Additionally, the shift in the band at 1447 cm^{-1} is not large enough to indicate Lewis sites (electron acceptance) [10]. Furthermore, a model reaction for OMS materials was conducted using dehydration of ethanol. This reaction did not show any detectable conversion (Fig. S7) because it depends on the presence of Brønsted or Lewis acid sites forming mainly ethylene or diethyl ether products [51]. Thus, these results corroborated the presence of only hydrogen-bonding sites in these materials.

Once the nature and the total number of sites were disclosed, the number of sites accessed by pyridine was examined with different experiments. First, Py-TPD was employed, which took into consideration the mass losses associated with desorption of water and pyridine in separate experiments, as detailed in the supplementary material [52]. The unique profiles of the TG/DTG curves of all OMS samples (Fig. 4) show a mass loss attributed to the release of physically adsorbed water (up to approximately 100 °C) and another loss between 100 and 350 °C due to pyridine desorption. The range of pyridine desorption on the OMS materials was much lower than that of other catalysts with stronger acid sites [30, 50, 51]. To ensure that the assignment of desorption in the TG experiment was correct, Py-TPD/MS was conducted under similar conditions (e.g., MCM-41). It could be seen (Fig. S8) that there was simultaneous desorption of

Table 3 Calculated number of Si–OH groups and the number of Py by TG methods for OMS materials

OMS	n_{OH} (mmol g^{-1}) ^a	α_{OH} (OH nm^{-2}) ^b	n_{Py} (mmol g^{-1})	α_{Py} (Py nm^{-2})
FDU-12	3.23	2.89	0.84	0.75
SBA-16	3.36	2.87	0.71	0.61
MCM-41	2.92	1.59	1.25	0.68
SBA-15	5.14	4.52	0.68	0.60

^a $n_{OH} = 2H_2O = 2(W_i - W_f)/100 MM_{H_2O}$, where W_i and W_f are the mass losses (wt%) in the temperature range (110–950 °C) and MM_{H_2O} is the water molar mass

^bThe number of OH groups (α_{OH}) per 1 nm^2 was calculated from the equation: $\alpha_{OH} = n_{OH} NA 10^{-18}/S_{BET}$, where: n_{OH} ($10^{-3} \times mmol g^{-1}$); NA —Avogadro constant, S_{BET} —OMS specific surface area obtained by BET method ($m^2 g^{-1}$), 10^{-18} —conversion factor from m^2 to nm^2

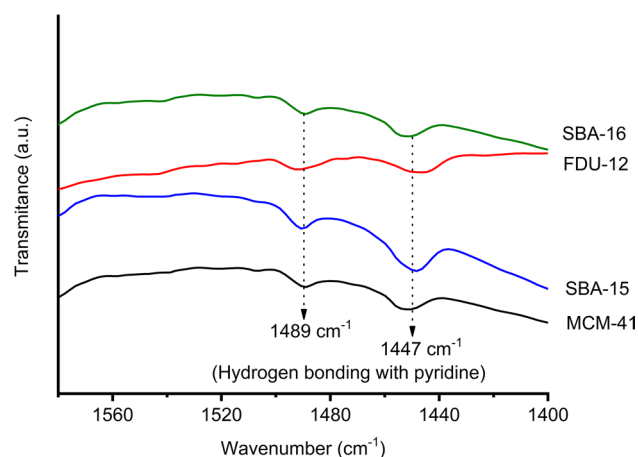


Fig. 3 FT-IR spectra of pyridine adsorbed on OMS: SBA-16, FDU-12, SBA-15, and MCM-41

Py and water in the same region, which confirmed that not all Si–OH sites of OMS reacted with pyridine during its adsorption.

This was reinforced by the quantitative calculation of the total number of Py molecules desorbed (n_{Py}) from accessed sites (Table 3, column 4). The n_{Py} is lower than n_{OH} , which corroborates the results of Py-TPD/MS experiments. There are a number of reasons that could lead to site concentrations obtained by a probe molecule (n_{Py}) being lower than the actual number of OH groups (n_{OH}) on the OMS inner surface, e.g., inactive hydroxyl groups and steric interactions between adjacent probe molecules that preclude an OH site from being accessible [53]. Thus, the data confirm those reasons and agree with others.

The data in Table 3 account for the number of sites on OMS accessible to pyridine, but equally important would be to know if they are homogeneous and have similar strength. Enthalpy has been used as an important measure of acid strength, providing a temperature-independent relative acidity scale [54–56]. Application of microcalorimetry in liquid phase in the preparation and design of new catalysts has shown great quantitative merit in that the nature and energy of adsorbed species can be addressed [57]. It is important to note that titration in liquid phase makes possible to discriminate the acid strength more accurately than in conventional gas–solid phase titration [58–60]. Differences between intrinsic and effective acidity that surface acidic groups of a catalyst present in a liquid is an important issue in the relationship between acidity and activity [59], which is addressed by slurry calorimetry.

The calorimetric analysis was based on obtaining data from the curves of heat evolved versus total amount of pyridine added, which was plotted as enthalpy versus total pyridine added for an easier comparison (Fig. S9). The model employed linearization of straight portions of the original

curve, assuming a two-acid site present in a solid acid, based on the best fitting parameters for these OMS materials. Then, the strength of the acid sites of OMS was probed by liquid-phase microcalorimetry of pyridine adsorption. Enthalpies are calculated as a measure of acid strength by measuring the heat of interaction between a diluted probe base and the acid sites of a solid in a noninteracting solvent. The average strength and number of sites in the mesoporous silicas are reported in Table 4. It should be noted that the total amount of pyridine (n_{Py}) obtained by Py-TPD is similar to that obtained by microcalorimetry (i.e., $n_1 + n_2$, Table 4, column 6). This confirms that both experiments assessed approximately the same sites on each OMS material.

Based on the strength of the most acidic sites, the order of OMS acidity was $FDU-12 > MCM-41 \geq SBA-16 > SBA-15$, with $-\Delta H_1 = 74.5, 66.8, 66.1$ and 36.8 kJ mol^{−1}, respectively. The acidity order is approximately the same as the order of accessibility of pyridine to the silanol groups (α_{Py}) for both Py-TPD and calorimetry measurements, as well as the relative amount of silanol groups (Si–OH or $Q^3 + Q^2$) inside the pores and on the surface of the OMS materials (Table 2). Although all pores are large enough to permit the entrance of pyridine (kinetic diameter = 0.54 nm), the presence of different amounts and the location of the most acidic sites for its hydrogen bonding is not the same. These are probably related to the synthesis conditions, the geometric environment of OMS that leads to their distribution, the accessibility (diffusion) inside the pores and the presence of relative amount of microporous in the OMS. Additionally, pyridine molecules could be bonded to some extent the external surface area of the OMS, which has other chemical environments with weaker strength. The most acidic sites are those with the highest potential energy surface (negative free energy) inside the pores [19, 20, 22]. The nature of the most reactive sites for hydroxylated silica surfaces (Fig. 5) are those with three mutually hydrogen-bonded hydroxyl groups [55, 56]. Nonetheless, one should be aware that the strength of surface groups on OMS materials can be tuned either by different morphologies, grafting silyls or other organic functional groups, or the addition of heteroatoms (e.g., Al, Ni, V) [10, 19, 21, 58, 61, 62]. Thus, it is essential to understand the pure OMS acidity for adequate modification.

The microcalorimetry of pyridine adsorption has proven to be an efficient tool to differentiate the strength of sites in many solid acids [52, 55, 56, 63]. Chronister et al. [56] calculated the thermodynamic data from Cal-Ad analysis of silica gel, which was treated at 28 °C for 12 h under vacuum. A two-site model was proposed with the following strength and quantities: $-\Delta H_1 = 52.7$ and $-\Delta H_2 = 22.2$ kJ mol^{−1}; $n_1 = n_2 = 0.86$ mmol g^{−1}. Under another hydration condition (200 °C, 12 h under vacuum), the enthalpy value for the strongest site ($-\Delta H_1$) was 23 kJ mol^{−1}. These results confirm how important the thermal treatment is to preserve the

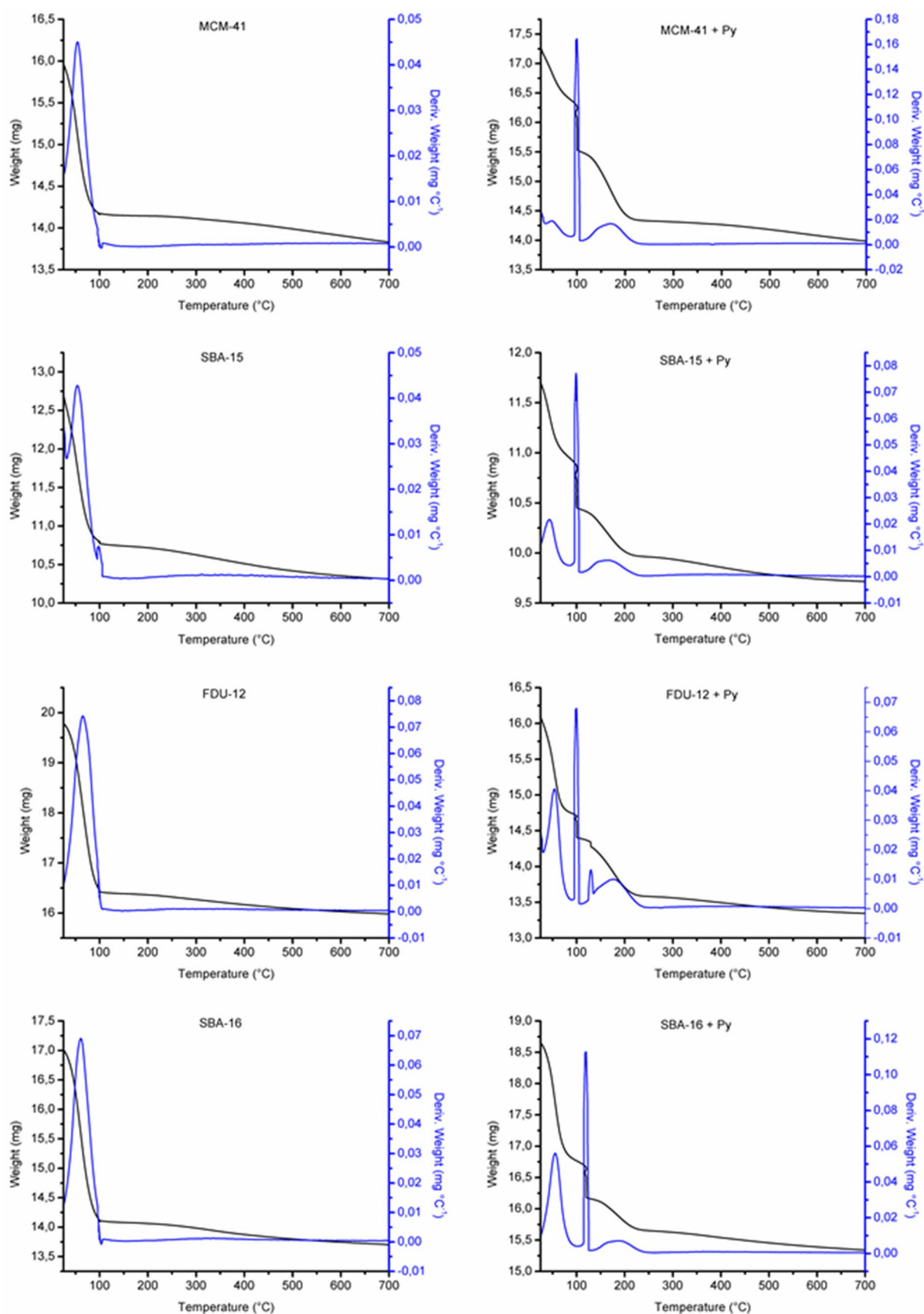


Fig. 4 Curves obtained by TG/DTG of OMS: MCM-41; SBA-15; FDU-12 and SBA-16 before (left) and after (right) adsorption of pyridine (Py-TPD)

Table 4 The total number of acid sites (n_{py}) obtained by Py-TPD, average enthalpy ($-\Delta H_1$ and $-\Delta H_2$), number of sites ($n_T = n_1 + n_2$) and density of adsorbed Py (α_{py}) obtained by microcalorimetry of pyridine adsorption, considering a two-site model reaction

OMS	$-\Delta H_1$ (kJ/mol)	n_1 (mmol/g)	$-\Delta H_2$ (kJ/mol)	n_2 (mmol/g)	n_T (mmol/g)	α_{py} (Py nm $^{-2}$)
FDU-12	74.5	0.05	56.2	0.62	0.67	0.60
SBA-16	66.1	0.05	58.6	0.55	0.60	0.51
MCM-41	66.8	0.10	45.8	0.91	1.01	0.55
SBA-15	36.8	0.08	24.3	0.38	0.46	0.40

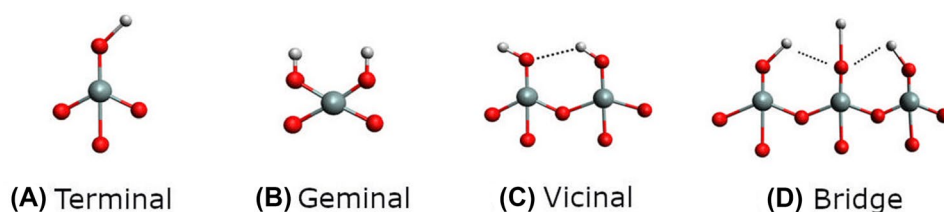
The standard deviations for $-\Delta H_1$ and $-\Delta H_2$ were ± 1 kJ mol $^{-1}$, and those for n_1 and n_2 were ± 0.01 and 0.03 mmol g $^{-1}$, respectively, based on triplicate experiments. For $-\Delta H_1$, the value was obtained by initial additions of pyridine in the titration using the limiting reagent approximation

nature of silanol groups on the surface. Considering that for all studied OMS materials, the total number of acid sites reacting with pyridine is lower than the total number of available silanols on the solids, it may indicate that once the first pyridine molecules reach the most reactive sites, the following molecules may experience steric hindrance to react with the remaining silanol groups. Moreover, as observed by the number of the strongest sites (n_1), there are fewer poly-hydrogen-bonded silanols (bridges). Figure 5 shows the arrangements of silanol groups on silicate materials. Those bridge silanols give rise to the strongest binding enthalpies of hydrogen-bonded silanols (Fig. 5d) that are stronger acids than the mono-hydrogen-bonded silanols, i.e., vicinal (Fig. 5c). Different pore structures, crystallinities and distributions of chemical environments demonstrate that there is a distinction between the accessibility and strength of the sites.

The enthalpy values of the first and second sites allow us to assign the nature of the sites reacted with pyridine for each OMS. These results may be inferred based on a comparison with silica gel. Site one is related to pyridine hydrogen bonded to poly-hydrogen-bonded silanols (bridge Si–OH, Fig. 5d), whereas site two is related to mono-hydrogen-bonded silanols (vicinal Si–OH, Fig. 5c), except for SBA-15, which is probably related to mono-hydrogen-bonded silanols.

The higher enthalpies for the strongest sites (site 1) than for silica gel are explained by the highly polar silanol groups formed inside the pores of OMS, which expose the OH mainly on the mesoporous walls due to the rigidity of their framework in agreement with ^{29}Si MAS NMR data. The

confinement effect of the structure's silanol groups within the pores will increase the O–H bond distance. In fact, this is one of the factors analyzed to evaluate accessibility, since the calculated chemical environments suggest this behavior, which strengthens the hydrogen bonding interaction with pyridine. The small differences in these distances probably caused the differences among the OMS materials. For SBA-15, the smaller enthalpy value ($-\Delta H_1 = 36.8$ kJ mol $^{-1}$) indicated that either the inner Si–OH are much more uniform in distribution or access to the strongest sites was precluded. This OMS has a significant amount of microporosity, and reactions with the most acidic sites might have been blocked by the initial pyridine entrance, as we explained before. Nonetheless, based on many reports in the literature [21, 23] that attribute no acidity to SBA-15 or even SBA-16, the hypothesis of a mixture of mono-hydrogen-bonded or even isolated silanols distribution may play a role, as well as morphology of OMS material in adsorptive process [64]. It has been confirmed that a highly interconnected (3D-mesopore network for SBA-15 showed real constrictions and dead ends in the supposedly uniform cylindrical pores in the primary pore system [65]. Thus, both effects are probably accounting for the final lower average strength of SBA-15 sites. An important difference between the pore structures of SBA-15 and MCM-41 is just that the pore walls contain these micropores and narrow mesopores, which is characteristic of synthesis with triblock copolymers [66]. The relatively high micropore volume and surface area of FDU-12, SBA-16 and MCM-41 indicate that a higher density of accessible silanols may be present inside their pores. The strongest sites observed for FDU-12 and SBA-16 suggest that the access is

Fig. 5 Different arrangements of Si–OH groups on silicate materials

facilitated by the largest pore system of windows and cages in this cubic structure. The same is valid for MCM-41, but in this case the 1D-channel system does not have much diffusion restrictions.

The strength and distribution of the hydrogen bonding acid sites discussed here are quite consistent with the results of other spectroscopic experiments in the literature [20]. MCM-41 and SBA-15 have been studied by multinuclear (^1H , ^{15}N , ^2D and ^{29}Si) solid-state NMR techniques using pyridine- ^{15}N . In this work, the majority of isolated silanol groups were confirmed to be in the inner surface of their pores, which were hydrogen bonded to pyridine at low coverage. ^{15}N MAS NMR spectra at low temperatures (-150°C) showed that pyridine can quickly jump among the silanols at room temperature, and the apparent n_{OH} was smaller than the real value. By ^1H MAS NMR, it was demonstrated that most silanol groups arose from inner surfaces (pores) but not from walls or small pores, which were not accessible to pyridine. It also showed that there were small variations in the H–N distances from the hydrogen bonds of silanol to pyridine detected by ^{15}N MAS NMR as broadness of lines, depending on the molecular sieve. However, there is not enough resolution in the MAS NMR spectra to detect chemical shifts of the possible different sites on those pores. Thus, in this work, we demonstrated that microcalorimetry with diluted pyridine was able to detect these small changes, showing average enthalpies that depend on the silanol OMS environment. The silanol groups are not able to protonate pyridine, forming pyridinium, a result that agrees with FT-IR measurements and *ab initio* calculations [67, 68].

In a recent paper, Velthoen et al. developed a method based on pyridine adsorbed on silica matrices with different strengths (silica, alumina, amorphous silica-alumina and zeolite Y) using reflectance UV–Vis spectroscopy [69]. The method allowed us to distinguish different absorption bands based on different pyridine adsorption modes. The bonds related to pyridine electronic transitions could be associated with the strength of surface species on surface of the catalyst. Compared to the traditional FT-IR method using adsorbed pyridine, which can easily distinguish Brønsted and Lewis acid sites, the UV–Vis method could distinguish better in nature and strength between weakly acidic surface hydroxyl groups (H-bonding sites) bonded to pyridine. We also observed this effect in our experimental FT-IR, since all four studied OMS showed similar spectra for pyridine adsorbed. Thus, compared to our microcalorimetric measurements, the UV–Vis method might be an alternative for in-depth characterization of solid acids with sites with different strengths.

Models of cylindrical pores using fused tridymite fragments have been proposed to accommodate data concerning the number of silanol groups [20, 28]. Based on these models and our results, we can suggest a qualitative picture

of the arrangement of the different Si–OH groups inside cylindrical and cage-like pores (Fig. 6). This model proposes the presence of a relatively rough inner pore surface with a few highly hydroxylated silanol groups that are responsible for the strongest sites in the OMS materials, as detected by microcalorimetry. In addition, the geminal and terminal (isolated) silanols are also present on the pore inner surface of OMS (Q^2 and Q^3 signals of ^{29}Si MAS NMR spectra), which contributes to decreasing the strength and hence the average enthalpies of the second site.

4 Conclusions

In this report, FDU-12, MCM-41, SBA-16 and SBA-15 were synthesized using minor modifications of verified methods in the literature. The produced and characterized materials have well-defined pores of long-range structural ordering. Donor–acceptor properties were assessed by calculating the surface Si–OH and Py densities. The nature of the Si–OH on these materials was confirmed as hydrogen-bonding sites using FT-IR of pyridine adsorption. Additionally, a model reaction of ethanol dehydration at 350°C showed negligible activity for those OMSs, confirming that Brønsted or Lewis sites were absent under those conditions. The number of moles of pyridine adsorbed (n_{Py}) was less than the number of hydroxyl groups (n_{OH} , maximum reactive sites) for all OMS, which might indicate steric hindrance between adjacent pyridine molecules that precludes some Si–OH sites from being accessible. It was determined by slurry microcalorimetry in cyclohexane of diluted pyridine adsorption that the synthesized OMS samples have two different types of active sites and are stronger than those of pure silica gel. The polar silanol groups formed inside the pores of OMS expose the OH mainly on the mesoporous walls because the rigidity of their framework coupled to the confinement effect. This increases the O–H bond distance, which strengthens the hydrogen bonding interaction with pyridine. The small differences in these distances probably caused the strength differences among the OMS materials. Pyridine reacts first with the most acidic silanol groups (bridge), which are related to three adjacent groups that can bind to hydrogen and are located within the mesopores. The second site, which is much more numerous, corresponded to monohydrogen-bonded silanol (vicinal). The obtained enthalpy data showed that the strength of both sites was in the order $\text{FDU-12} > \text{MCM-41} \geq \text{SBA-16} > \text{SBA-15}$. This order is similar to the distribution of pyridine (αPy) and SiOH groups ($Q^3 + Q^2$). Based on models proposed in the literature and our results, we suggest qualitative illustrations of the arrangement of the different Si–OH groups inside the pores. The pores present a partially rough inner surface

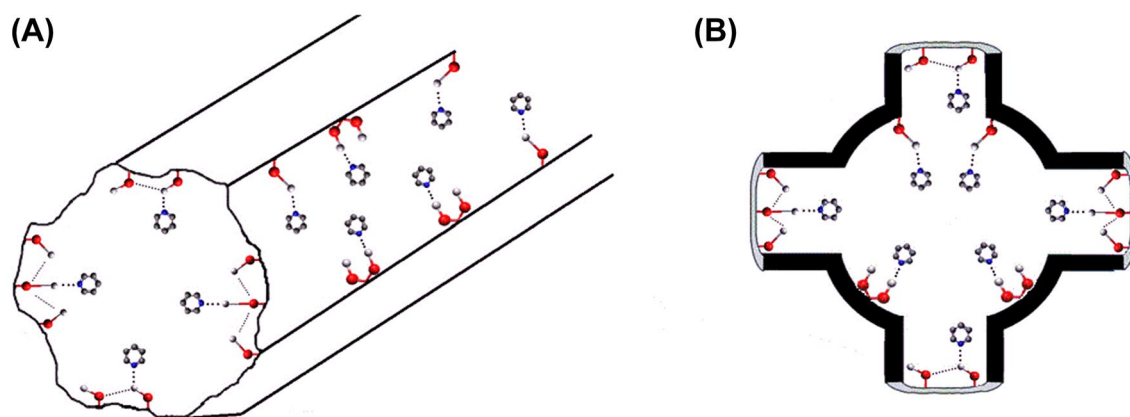


Fig. 6 General qualitative schematic model of OMS pores comprising H-acceptor silanols in a rough inner pore wall surface bonded to Py for **a** cylindrical and **b** cage-like pores

with a few highly hydroxylated silanol groups that are responsible for the strongest sites in the OMS materials. Additionally, a higher number of vicinal silanols compose the majority of the second strongest sites. Complementing the surface structure, geminal and terminal silanols are present on the inner pores and external surfaces of OMS.

Acknowledgements We acknowledge CNPq (Grant n° 307091/2018-0 and 307845/2019-2), CAPES (Grant n° 001) for research and graduate student scholarships and the financial support provided by DPI/IQ/UnB, MCTIC/CNPq (Grant n° 480165/2013-0 and 484384/2012-0), CAPES, FAPDF (Grant n° 0193.001799/2017 and 0193.001348/2016), FINATEC, FINEP/CTPetro/CTInfra, and Petrobras. Thanks CAPES for the postdoctoral fellowship for LCCS, and to CNPq for the research fellowship for MCAF. Also, LCCS wants to thank INCT 2014—nanotecnologia farmacêutica: uma abordagem transdisciplinar, Proc. n° 2014/50928-2, NanoSight NS300, FAPESP Proc. 17/17075-4. In addition, we would like to thank Dr. Tatiane Oliveira dos Santos from Laboratório Multiusuário de Microscopia de Alta Resolução (LabMic) at IF/UFG-Brazil for TEM measurements.

Author contributions MRA performed and participated in most of the experimental work as part of her PhD dissertation (e.g., synthesis of MCM-41 and SBA-15; thermogravimetric analysis, acquisition of ^{29}Si MAS and CP/MAS NMR spectra; textural data). MFP helped to obtain FT-IR spectra, H_2O -TPD and Py-TPD data using TG/DTG. EFF designed and conducted the microcalorimetric experiments. PTA design and helped to obtain H_2O -TPD/MS and Py-TPD/MS data, as well as the TEM images. MCH Clemente designed and run all ethanol dehydration reactions. GAVM helped to obtain and deconvolute ^{29}Si MAS and CP/MAS spectra. LCCS, MCAF, and ATS helped in the synthesis of FDU-12, SBA-15, and SBA-16, designed, conducted, and interpreted the SAXS experiments. SCLD designed and discussed the accessibility and acidity characterization of the materials. JAD coordinated the work and wrote the first drafts of the paper. All authors assisted in article writing revision, data interpretation and discussion of the results.

Compliance with ethical standards

Conflict of interest The authors declare no competing financial or any other conflict of interest.

References









1. C.T. Kresge, M.E. Leonowicz, W.J. Roth, J.C. Vartuli, J.S. Beck, *Nature* **359**, 710–712 (1992). <https://doi.org/10.1038/359710a0>
2. J.S. Beck, J.C. Vartuli, W.J. Roth, M.E. Leonowicz, C.T. Kresge, K.D. Schmitt, C.T.W. Chu, D.H. Olson, E.W. Sheppard, S.B. McCullen, J.B. Higgins, J.L. Schlenker, *J. Am. Chem. Soc.* **114**, 10834–10843 (1992). <https://doi.org/10.1021/ja00053a020>
3. A.J. Schwanke, A.P.B. Santos, L. Bieseki, P.R.P. Campos, S.B.C. Pergher, *Materiais Mesoporosos: Um Caminho Acessível*, 1st edn. (Editora da UFRN - Edufrn, Natal, 2016), pp. 10–50
4. Q. Wang, D.F. Shantz, *J. Solid State Chem.* **181**, 1659–1669 (2008). <https://doi.org/10.1016/j.jssc.2008.06.015>
5. V. Meynen, P. Cool, E.F. Vansant, *Microporous Mesoporous Mater.* **125**, 170–223 (2009). <https://doi.org/10.1016/j.micromeso.2009.03.046>
6. Y. Li, J. Shi, *Adv. Mater.* **26**, 3176–3205 (2014). <https://doi.org/10.1002/adma.201305319>
7. T. Lehmann, T. Wolff, C. Hamel, P. Veit, B. Garke, A. Seidel-Morgenstern, *Microporous Mesoporous Mater.* **151**, 113–125 (2012). <https://doi.org/10.1016/j.micromeso.2011.11.006>
8. J. Weglarski, J. Datka, H. He, J. Klinowski, *J. Chem. Soc. Farad. Trans.* **92**, 5161–5164 (1996). <https://doi.org/10.1039/ft9969205161>
9. H. Landmesser, H. Kosslick, U. Kürschner, A. Rolf Fricke, *J. Chem. Soc. Farad. Trans.* **94**, 971–977 (1998). <https://doi.org/10.1039/a707879j>
10. A. Corma, *Chem. Rev.* **97**, 2373–2420 (1997). <https://doi.org/10.1021/cr960406n>
11. L. Washmon-Kriel, V.L. Jimenez, K.J. Balkus, *J. Mol. Catal. B* **10**, 453–469 (2000). [https://doi.org/10.1016/S1381-1177\(99\)00123-X](https://doi.org/10.1016/S1381-1177(99)00123-X)
12. N. Carlsson, H. Gustafsson, C. Thörn, L. Olsson, K. Holmberg, B. Åkerman, *Adv. Colloid Interface Sci.* **205**, 339–360 (2014). <https://doi.org/10.1016/j.cis.2013.08.010>
13. A. Vinu, V. Murugesan, O. Tangermann, M. Hartmann, *Chem. Mater.* **16**, 3056–3065 (2004). <https://doi.org/10.1021/cm049718u>
14. S.M.L. Santos, J.A. Cecilia, E. Vilarrasa-García, C. García-Sancho, I.J. Silva Jr., E. Rodríguez-Castellón, D.C.S. Azevedo, *Microporous Mesoporous Mater.* **260**, 146–154 (2018). <https://doi.org/10.1016/j.micromeso.2017.10.044>
15. Z. Zhou, M. Hartmann, *Chem. Soc. Rev.* **42**, 3894–3912 (2013). <https://doi.org/10.1039/c3cs60059a>

16. A. Maleki, H. Kettiger, A. Schoubben, J.M. Rosenholm, V. Ambrogio, M. Hamidi, J. Control. Release. **262**, 329–347 (2017). <https://doi.org/10.1016/j.jconrel.2017.07.047>
17. N. Vilaça, A.F. Machado, F. Morais-Santos, R. Amorim, A. Patrícia Neto, E. Logodin, M.F.R. Pereira, M. Sardo, J. Rocha, P. Parpot, A.M. Fonseca, F. Baltazar, I.C. Neves, RSC Adv. **7**, 13104–13111 (2017). <https://doi.org/10.1039/C7RA01028A>
18. F. Farjadian, S. Azadi, S. Mohammadi-Samani, H. Ashrafi, A. Azadi, Heliyon. **4**, e00930 (2018). <https://doi.org/10.1016/j.heliyon.2018.e00930>
19. X.S. Zhao, G.Q. Lu, A.K. Whittaker, G.J. Millar, H.Y. Zhu, J. Phys. Chem. B. **101**, 6525–6531 (1997). <https://doi.org/10.1021/jp971366>
20. I.G. Shenderovich, G. Buntkowsky, A. Schreiber, E. Gedat, S. Sharif, J. Albrecht, N.S. Golubev, G.H. Findenegg, H.-H. Limbach, J. Phys. Chem. B. **107**, 11924–11939 (2003). <https://doi.org/10.1021/jp0349740>
21. J.M.R. Gallo, C. Bisio, G. Gatti, L. Marchese, H.O. Pastore, Langmuir **26**, 5791–5800 (2010). <https://doi.org/10.1021/la903661q>
22. P.R.S. Braga, A.A. Costa, J.L. de Macedo, G.F. Ghesti, M.P. de Souza, J.A. Dias, S.C.L. Dias, Microporous Mesoporous Mater. **139**, 74–80 (2011). <https://doi.org/10.1016/j.micromeso.2010.10.020>
23. S.S. Enumula, V.R.B. Gurram, R.R. Chada, D.R. Burri, S.R.R. Kamaraju, J. Mol. Catal. A **426**, 30–38 (2017). <https://doi.org/10.1016/j.molcata.2016.10.032>
24. J. Fan, C. Yu, F. Gao, J. Lei, B. Tian, L. Wang, Q. Luo, B. Tu, W. Zhou, D. Zhao, Angew. Chem. Int. Ed. **42**, 3146–3150 (2003). <https://doi.org/10.1002/anie.200351027>
25. M. Kruk, C.M. Hui, Microporous Mesoporous Mater. **114**, 64–73 (2008). <https://doi.org/10.1016/j.micromeso.2007.12.015>
26. D. Zhao, Science **279**, 548–552 (1998). <https://doi.org/10.1126/science.279.5350.548>
27. D. Zhao, Q. Huo, J. Feng, B.F. Chmelka, G.D. Stucky, J. Am. Chem. Soc. **120**, 6024–6036 (1998). <https://doi.org/10.1021/ja974025i>
28. S.A. Kozlova, S.D. Kirik, Microporous Mesoporous Mater. **133**, 124–133 (2010). <https://doi.org/10.1016/j.micromeso.2010.04.024>
29. V.V. Potapov, L.T. Zhuravlev, Glas. Phys. Chem. **31**, 661–670 (2005). <https://doi.org/10.1007/s10720-005-0111-z>
30. P.R.S. Braga, A.A. Costa, E.F. de Freitas, R.O. Rocha, J.L. de Macedo, A.S. Araujo, J.A. Dias, S.C.L. Dias, J. Mol. Catal. A **358**, 99–105 (2012). <https://doi.org/10.1016/j.molcata.2012.03.002>
31. NIST Webbook. <https://webbook.nist.gov>, 2020. Accessed 31 March 2020.
32. R.M. Grudzien, B.E. Grabicka, M. Jaroniec, J. Mater. Chem. **16**, 819–823 (2006). <https://doi.org/10.1039/B515975J>
33. L.C.C. da Silva, Síntese, caracterização e potenciais aplicações de materiais nanoporosos altamente ordenados, Universidade de São Paulo (2007). <https://doi.org/10.11606/T.46.2007.tde-03082007-094353>
34. M. Thommes, K. Kaneko, A.V. Neimark, J.P. Olivier, F. Rodriguez-Reinoso, J. Rouquerol, K.S.W. Sing, Pure Appl. Chem. **87**, 1051–1069 (2015). <https://doi.org/10.1515/pac-2014-1117>
35. M. Ide, M. El-Roz, E. De Canck, A. Vicente, T. Planckaert, T. Bogaerts, I. Van Driessche, F. Lynen, V. Van Speybroeck, F. Thybault-Starzyk, P. Van Der Voort, Phys. Chem. Chem. Phys. **15**, 642–650 (2013). <https://doi.org/10.1039/c2cp42811c>
36. K.J.D. MacKenzie, M.E. Smith (eds.), *Multinuclear Solid-State NMR of Inorganic Materials*, 1st edn. (Pergamon Materials Series, Oxford, 2002), pp. 201–260
37. C.-M. Yang, B. Zibrowius, W. Schmidt, F. Schüth, Chem. Mater. **16**, 2918–2925 (2004). <https://doi.org/10.1021/cm049526z>
38. C.-Y. Chen, H.-X. Li, M.E. Davis, Microporous Mater. **2**, 17–26 (1993). [https://doi.org/10.1016/0927-6513\(93\)80058-3](https://doi.org/10.1016/0927-6513(93)80058-3)
39. L.T. Zhuravlev, Colloids Surf. A **173**, 1–38 (2000). [https://doi.org/10.1016/S0927-7757\(00\)00556-2](https://doi.org/10.1016/S0927-7757(00)00556-2)
40. M. Barczak, New J. Chem. **42**, 4182–4191 (2018). <https://doi.org/10.1039/C7NJ04642A>
41. P. Ngene, S.F.H. Lambregts, D. Blanchard, T. Vegge, M. Sharma, H. Hagemann, P.E. de Jongh, Phys. Chem. Chem. Phys. **21**, 22456–22466 (2019). <https://doi.org/10.1039/C9CP04235K>
42. I. Gillis-D'Hammers, I. Cornelissens, K.C. Vrancken, P. Van Der Voort, E.F. Vansant, F. Daelemans, J. Chem. Soc. Farad. Trans. **88**, 723–727 (1992). <https://doi.org/10.1039/ft9928800723>
43. V.L. Zholobenko, D. Plant, A.J. Evans, S.M. Holmes, Microporous Mesoporous Mater. **44–45**, 793–799 (2001). [https://doi.org/10.1016/S1387-1811\(01\)00262-1](https://doi.org/10.1016/S1387-1811(01)00262-1)
44. A. Corma, V. Fornes, M.T. Navarro, J. Perezpariente, J. Catal. **148**, 569–574 (1994). <https://doi.org/10.1006/jcat.1994.1243>
45. C. Jia, P. Beaunier, P. Massiani, Microporous Mesoporous Mater. **24**, 69–82 (1998). [https://doi.org/10.1016/S1387-1811\(98\)00144-9](https://doi.org/10.1016/S1387-1811(98)00144-9)
46. D.W. Sendorf, G.E. Maciel, J. Phys. Chem. **87**, 5516–5521 (1983). <https://doi.org/10.1021/j150644a041>
47. D.K. Murray, J. Colloid Interface Sci. **352**, 163–170 (2010). <https://doi.org/10.1016/j.jcis.2010.08.045>
48. R. Atluri, Z. Bacsik, N. Hedin, A.E. Garcia-Bennett, Microporous Mesoporous Mater. **133**, 27–35 (2010). <https://doi.org/10.1016/j.micromeso.2010.04.007>
49. V.I. Lygin, Russ. J. Gen. Chem. **71**, 1368–1372 (2001). <https://doi.org/10.1023/A:1013997717868>
50. R.S. Drago, S.C. Dias, M. Torrealba, L. de Lima, J. Am. Chem. Soc. **119**, 4444–4452 (1997). <https://doi.org/10.1021/ja9633530>
51. M.C.H. Clemente, G.A.V. Martins, E.F. de Freitas, J.A. Dias, S.C.L. Dias, Fuel **239**, 491–501 (2019). <https://doi.org/10.1016/j.fuel.2018.11.026>
52. F.C.G. de Mattos, E.N.C.B. de Carvalho, E.F. de Freitas, M.F. Paiva, G.F. Ghesti, J.L. de Macedo, S.C.L. Dias, J.A. Dias, J. Braz. Chem. Soc. **28**, 336–347 (2017). <https://doi.org/10.5935/0103-5053.20160183>
53. A.I. Biaglow, D.J. Parrillo, G.T. Kokotailo, R.J. Gorte, J. Catal. **148**, 213–223 (1994). <https://doi.org/10.1006/jcat.1994.1203>
54. R.S. Drago, J.A. Dias, T.O. Maier, J. Am. Chem. Soc. **119**, 7702–7710 (1997). <https://doi.org/10.1021/ja9639123>
55. F.J. Feher, D.A. Newman, J. Am. Chem. Soc. **112**, 1931–1936 (1990). <https://doi.org/10.1021/ja00161a044>
56. C.W. Chronister, R.S. Drago, J. Am. Chem. Soc. **115**, 4793–4798 (1993). <https://doi.org/10.1021/ja00064a045>
57. P. Carniti, A. Gervasini, in *Calorimetry and Thermal Methods in Catalysis*, vol. 154, by ed. A. Auroux (Springer Series in Material Science, London, 2013), pp. 552–569.
58. A. Gervasini, A. Auroux, Thermochim. Acta **567**, 8–14 (2013). <https://doi.org/10.1016/j.tca.2013.03.028>
59. P. Carniti, A. Gervasini, S. Biella, A. Auroux, Chem. Mater. **17**, 6128–6136 (2005). <https://doi.org/10.1021/cm0512070>
60. E.F. Kozhevnikova, I.V. Kozhevnikov, J. Catal. **224**, 164–169 (2004). <https://doi.org/10.1016/j.jcat.2004.03.001>
61. Y. Liu, Catalysts **8**(537), 1–14 (2018). <https://doi.org/10.3390/catal8110537>
62. H.-P. Lin, L.-Y. Yang, C.-Y. Mou, S.-B. Liu, H.-K. Lee, New J. Chem. **24**, 253–255 (2000). <https://doi.org/10.1039/b001858i>
63. F.A.C. Garcia, V.S. Braga, J.C.M. Silva, J.A. Dias, S.C.L. Dias, J.L.B. Davo, Catal. Lett. **119**, 101–107 (2007). <https://doi.org/10.1007/s10562-007-9204-8>
64. S. Kingchok, S. Pornsuwan, J. Porous Mater (2020). <https://doi.org/10.1007/s10934-020-00932-x>
65. S.-J. Reich, A. Svidrytski, A. Höltzel, J. Florek, F. Kleitz, W. Wang, D. Hlushkou, U. Tallarek, J. Phys. Chem. C **122**, 12350–12361 (2018). <https://doi.org/10.1021/acs.jpcc.8b03630>

66. L. Giraldo, M. Bastidas-Barranco, J.C. Moreno-Piraján, *Colloids Surf. A* **496**, 100–113 (2016). <https://doi.org/10.1016/j.colsurfa.2015.10.049>
67. A. Jentys, K. Kleesstorfer, H. Vinek, *Microporous Mesoporous Mater.* **27**, 321–328 (1999). [https://doi.org/10.1016/S1387-1811\(98\)00265-0](https://doi.org/10.1016/S1387-1811(98)00265-0)
68. K. Marshall, G.L. Ridgewell, C.H. Rochester, J.J. Simpson, *Chem. Ind.* 775 (1974).
69. M.E.Z. Velthoen, S. Nab, B.M. Weckhuysen, *Phys. Chem. Chem. Phys.* **20**, 21647–21659 (2018)

Publisher's Note Springer Nature remains neutral with regard to jurisdictional claims in published maps and institutional affiliations.

Affiliations

Mayara R. Alves¹ · Mateus F. Paiva¹  · Pablo T. A. Campos¹ · Elon F. de Freitas¹  · Maria Clara H. Clemente¹  · Gesley Alex V. Martins¹  · Alceu T. Silveira Jr.² · Luis C. Cides da Silva³  · Marcia C. A. Fantini³  · Sílvia C. L. Dias¹  · José A. Dias¹ 

Mayara R. Alves
<http://www.labcat.unb.br>

Mateus F. Paiva
<http://www.labcat.unb.br>

Pablo T. A. Campos
<http://www.labcat.unb.br>

Elon F. de Freitas
<http://www.labcat.unb.br>

Maria Clara H. Clemente
<http://www.labcat.unb.br>

Gesley Alex V. Martins
<http://www.labcat.unb.br>

Alceu T. Silveira Jr.
alceu@iq.usp.br

Luis C. Cides da Silva
luisccides@gmail.com

Marcia C. A. Fantini
mfantini@if.usp.br

Sílvia C. L. Dias
<http://www.labcat.unb.br>

- ¹ Universidade de Brasília – Campus Universitário Darcy Ribeiro – Asa Norte - Instituto de Química - Laboratório de Catálise, Brasília, DF 70910-900, Brazil
- ² Instituto de Química, Universidade de São Paulo, Av. Prof. Lineu Prestes, 748 - Butantã, São Paulo, SP 05508-000, Brazil
- ³ Instituto de Física, Universidade de São Paulo, Cidade Universitária, Rua do Matão N° 1371, São Paulo, SP 05508-090, Brazil